Nonlinear Dyn
https://doi.org/10.1007/s11071-024-10719-3

RESEARCH

Modeling-free inversion-based iterative feedforward control of magneto-rheological dampers

Shuyou Yu · Shaoyu Sun · Jie Guo · Xinze Xu · Songlin Zhang · Ye Zhuang

Received: 8 April 2024 / Accepted: 25 November 2024

Abstract In this paper, a damping force tracking control strategy of magneto-rheological dampers with nonlinear and hysteresis characteristics is proposed, in which a modeling-free inversion-based iterative feedforward control (MIIFC) scheme is designed. The adopted MIIFC scheme utilizes only online input–output data of the controlled system, and achieves the desired performance by iterations. The property of disturbances or noises attenuation, i.e., convergence analysis is explicitly addressed accordingly. The validity of the adopted MIIFC scheme was verified by simulation experiments and hardware-in-the-loop tests on a seat suspension test rig installed with the magneto-rheological damper. The experimental results show that the desired damping force can be effectively tracked with the MIIFC scheme.

Keywords Iterative learning control · Magneto-rheological damper · Model-free · Tracking control · Seat suspension

S. Yu
National Key Laboratory of Automotive Chassis Integration and Bionics, Jilin University, Changchun 130025, China
e-mail: shuyou@jlu.edu.cn

Y. Zhuang (✉)
State Key Laboratory of Automotive Simulation and Control, Jilin University, Changchun 130025, China
e-mail: zhuangye@jlu.edu.cn

S. Yu · S. Sun · J. Guo · X. Xu · S. Zhang
Department of Control Science and Engineering, Jilin University, Changchun 130025, China
e-mail: sysun22@mails.jlu.edu.cn

J. Guo
e-mail: jieguo20@mails.jlu.edu.cn

X. Xu
e-mail: xuxz21@mails.jlu.edu.cn

S. Zhang
e-mail: songlin19@mails.jlu.edu.cn

1 Introduction

The magneto-rheological (MR) fluid is a typical smart material [15], whose shear yield stress is adjusted through the strength change of the external magnetic field. The adjustment process only takes a few milliseconds [1,15]. An MR damper has many advantages, for example, easy control, fast response, simple structure, low energy consumption, and large and continually adjustable scope [1,10]. Thus, MR damper is widely used in fields of vehicles, buildings, and medical treatment [1,5,10,15].

Modeling of MR damper can be roughly classified into parametric and non-parametric models. The parametric models include Bouc-Wen model [12,24], phenomenological model [3,8], and Dahl model [16], etc. Normally, an inverse model is chosen as feedforward controller of an MR damper [13,17,20] in order to obtain the required current in terms of the desired damping force and piston motion state [17,20]. The feedforward control has a simple control structure and fast response [13]. However, in general, it is difficult to obtain a parametric inverse model since there are many parameters to identify [17].

Non-parametric models adopt schemes of numerical fitting or data training by taking the displacement, velocity and current of an MR damper as inputs and the measured damping force as outputs to approximate dynamic characteristics directly. The accuracy of non-parametric models depends on the authenticity of the experimental data, which reflect the relationship between the displacement, velocity and the damping force. The typical non-parametric models of an MR damper contain polynomial model [19], neural network model [4], and fuzzy system [7], etc. The existence of disturbances [17] and continuously mechanical wear in shock absorber/damper test systems leads to a large number of complex constraints, which significantly reduces the robustness and adaptability of the system [14]. For example, factors such as load perturbations cause mismatches of the non-parametric neural network model [20], which affect the generalization ability of the neural network, and reduce the control accuracy of the inverse model accordingly.

In real-time control of seat suspension systems equipped with the magneto-rheological damper, an inverse model of the MR damper converts the desired damping force into control current [21], whose accuracy directly determines the tracking accuracy of inverse-model-based control methods. In order to deal with nonlinear hysteresis modeling, an iterative learning control scheme is proposed in [2], which treats the hysteresis nonlinearity as disturbances in the process of iteration. However, parameters of the iterative learning controller still depend on the specific dynamic characteristics of the MR damper. With the development of control theory, data-driven or model-free approach is proposed [22], which uses the input and output data of the plant to design controller directly.

In this paper, the modeling-free inversion-based iterative feedforward control (MIIFC) scheme proposed in [11] is successfully used on the damping force tracking control of an MR damper, whose design parameters only depend upon input–output data of the controlled system [23]. By using measured input–output data to update the inverse model at each iteration, the MIIFC scheme improves the quality of the inverse model accordingly. Furthermore, influences of disturbance/noise are explicitly addressed in the convergence analysis of the MIIFC scheme.

The organization structure of this paper is as follows: Sect. 2 introduces the MR damper experimental platform. Section 3 designs the modeling-free inversion-based iterative feedforward controller of the MR damper, and analyzes its convergence. Section 4 verifies the effectiveness of the MIIFC scheme by the damping force tracking experiment of the MR damper in Matlab/Simulink environment. In Sect. 5, physic experiments are conducted. Finally, conclusions are drawn.

2 System description

The experimental data selected in this paper are the input–output data of an MR damper measured on the seat suspension experimental system. The seat suspension experimental system equipped with an MR damper shown in Figs. 1 and 2 is employed.

The system consists of three main components, i.e., an electric motor power system, a data acquisition and control system, and a seat suspension system with sensors. The motor is manufactured by Yaskawa Electric Corporation of Japan, with a rated power of $400W$, a stroke of $200mm$, a rated output of $5.8kN$, and a maximum instantaneous output of $17.4kN$. The motor provides the actuating force for the seat suspension experimental system to simulate different road surfaces.

The hardware of the data acquisition and control system mainly consists of upper and lower industrial computers, data acquisition cards, and current drive boards. The upper computer uses Windows operating system, with an Intel Core i5 CPU, $250G$ memory and Matlab 2015a installed, mainly used for controller designing and data processing. The lower computer uses Dos operating system, with the same CPU type as the upper computer, and $8G$ running memory. The board card installed in the industrial computer is NI PCI-6229 M, which provides 32 analog input ports, 4 analog output ports and 48 digital input/output ports. The board card has an internal clock frequency of $80MHz$, two 32-bit counters/timers and digital triggering function, which can add sensors and voltage measurement functions. The control current of the MR damper is provided by a self-developed current drive board, which is powered by an $18-24V$ voltage. The drive board can output a control current based on the input voltage, with a maximum output current of $2A$. Damping control can

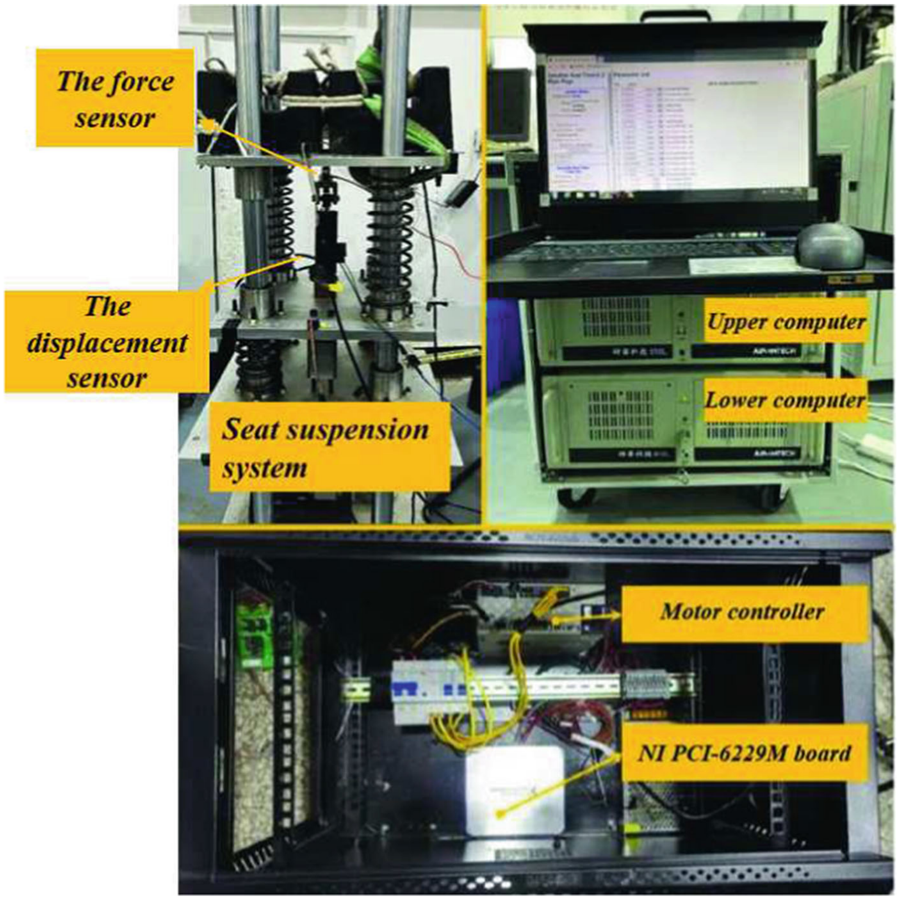

Fig. 1 Experimental setup

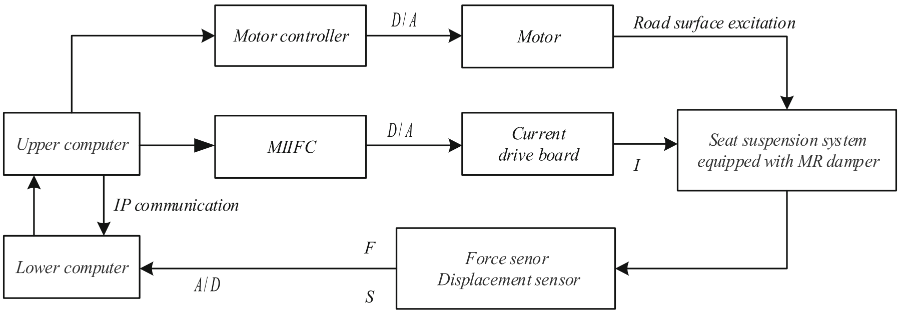

Fig. 2 The principle of seat suspension experimental system

be achieved by sending a voltage signal to the drive board.

The MR damper installed in the seat suspension experimental system is the RD-8041-1 from LORD Corporation. Two ADXL335 accelerometers are equipped to measure the sprung acceleration and unsprung acceleration, respectively. The displacement sensor used is R38S-6G05E for measuring the relative displacement of the piston rod for the MR damper, and the force sensor used is DMYH-106 for measuring the output damping force of the MR damper. According to the stroke of MR damper, the test amplitude is in the range of [−20 mm, 20 mm]. The displacement excitation is adopted in the experiment and the piston stroke is selected as sinusoidal signals with frequencies of 0.414 Hz, 1.043 Hz, 2.085 Hz, and 4.170 Hz, respectively. The corresponding maximum piston velocities for the four groups are 0.052 m/s, 0.131 m/s, 0.262 m/s, and 0.524 m/s, respectively, as shown in Table 1. The initial position of the piston rod is in the middle of

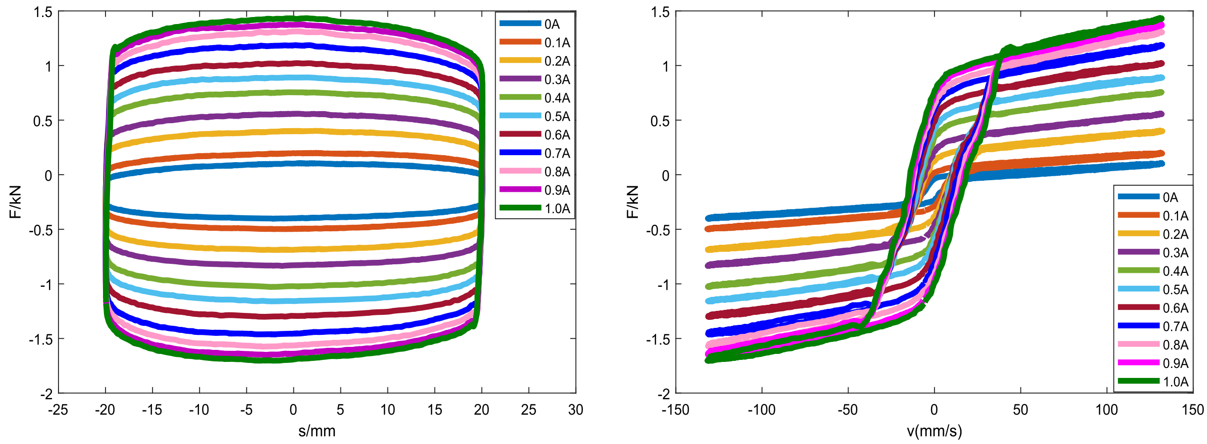

(a) curves of force-displacement. (b) curves of force-velocity.

Fig. 3 Characteristic curve of MR damper at the maximum velocity $v = 0.131$ m/s

Table 1 Input signal information

Frequency (Hz)	Dynamic stroke (mm)	Maximum speed of piston motion (m/s)
0.414	40	0.052
1.043	40	0.131
2.085	40	0.262
4.170	40	0.524

MR damper. The input current ranges from 0 to $1A$. In compliance with JB/T 13513-2018, the relationship between the piston motion speed, dynamic stroke, and frequency can be described as follows [6]:

$$v = \pi \cdot s \cdot f \tag{1}$$

The characteristics of the MR damper with the piston velocity of $0.131m/s$ is shown in Fig. 3. Figure 3a shows that the MR damper has good energy dissipation characteristics, i.e., the damping force increases with the increase of current at each excitation velocity. Figure 3b shows that the damping force of the MR damper has obvious hysteresis characteristics as the velocity changes, and the hysteresis phenomenon intensifies as the current increases.

From the above analysis of the external characteristics of MR damper, it can be seen that MR damper has not only good energy dissipation characteristics, but also obvious hysteresis characteristics. The control objective of the MR damper is to reduce the influence of hysteresis nonlinearity on system performance, allowing for quicker and more accurate tracking of the desired damping force.

3 Controller design

MR damper is a single-input single-output system. Damping force of an MR damper is generated by repeated movements of the piston rod in the cylinder barrel when the piston rod moves regularly. To some extent, the process of a damping force tracking control can be regarded as a kind of repetitive motion control, whose tracking performance can be gradually improved by iterations. The input and output data are directly used to construct the MIIFC scheme. The process of the identification of a system inversion is avoided, and errors caused by uncertainties or model-plant mismatches are attenuated.

The control structure is shown in Fig. 4, where $\mathrm{F}_{k-1,n}$ denotes the noise/disturbance at the $(k-1)th$ iteration, $\mathrm{F}_{k-1,r}$ denotes the output damping force at the $(k-1)th$ iteration, F_{k-1} denotes the output damping force, i.e., the output damping force mixed with measurement noise at the $(k-1)th$ iteration, F^* denotes the desired damping force and needs to be obtained by the current suspension motion state in each iteration. Note that the principle for determining F^* is to minimize the vertical acceleration of the sprung mass while keeping

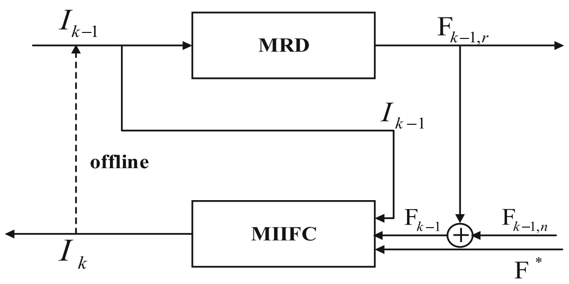

Fig. 4 MIIFC structure of MR damper

the dynamic stroke within the constrained range. I_{k-1} denotes the control current at the $(k-1)th$ iteration, I_k denotes the control current at the kth iteration, and MRD is the plant.

The control current is modified by the MIIFC scheme in terms of the last input current and output of the damping force in order to improve the tracking performance along iterations. The principle of the MIIFC scheme is expressed as follows:

$$I_k = \begin{cases} \alpha F_k^* , & k = 0 \\ \frac{I_{k-1}}{F_{k-1}} F_k^* , & while \ \ F_{k-1} \neq 0, \\ & and \ \ F_k^* \neq 0 , \ k \geq 1 \\ 0, & otherwise \end{cases} \tag{2}$$

where $k = 0, 1, 2 \cdots$ denotes the number of iterations.

The initial control I_0 of the MR damper is obtained by multiplying the desired damping force F_0^* by a preselected parameter α, which can be determined by trial-and-error, and needs to ensure that the output damping force follows the trend of the desired force. The initial output F_0 is obtained by implementing I_0 into the MRD. Thereafter, I_{k-1}/F_{k-1} and the control current I_k for the kth iteration are selected rather than constructing an inverse model. Note that at the start of the iterative process, the real damping force and the desired damping force from the previous iteration cannot be zero, as this would lead to undefined values in the algorithm. During the iterative process, however, the damping force may become zero, in which case no current is applied as the damper is inactive.

3.1 Convergence analysis

Denote δ as the ratio of the measurement noise $F_{k,n}$ to the desired damping force F_k^*, i.e.,

$$\delta = \frac{F_{k,n}}{F_k^*} \ . \tag{3}$$

When the piston rod moves repetitively according to certain principles, the current is the only tunable variable.

Denote G_d as the transfer function of the open-loop stable SISO system which is an intermediate term in the convergence analysis of the MIIFC scheme.

The terms of $F_{k,r}$ and F_k^* are given by:

$$F_{k,r} \ = \ I_k G_d \tag{4}$$
$$F_k^* \ = \ I_{k,d} G_d \tag{5}$$

where $I_{k,d}$ denotes the desired control current. Note that $I_{k,d}$ is an unknown term which is only used in the convergence analysis of the MIIFC scheme.

Theorem 1 [11] *Suppose that G_d is an open-loop stable SISO system, and consider the control law (2). Then, the ratio of the control current I_k to the desired current $I_{k,d}$ at the kth iteration is given by*

$$\frac{I_k}{I_{k,d}} = \frac{G_d}{G_d(1+S_k) + P_k/\alpha} \tag{6}$$

where P_k denotes the product of δ at frequencies from $\omega = 0$ to $\omega = k-1$ and S_k denotes the summation of the product P_k, i.e.,

$$P_k = \prod_{i=0}^{k-1} \frac{F_{i,n}}{F_i^*} \tag{7}$$

$$S_k = \begin{cases} 0 \, , & \text{while k} = 1 \\ \sum_j^{k-1} \prod_{i=1}^{j} \frac{F_{k-i,n}}{F_{k-i}^*} \ , & \text{while k} \geq 2 \, . \end{cases} \tag{8}$$

Lemma 1 *The convergence of the MIIFC scheme is guaranteed while $\delta < 0.5$.*

Proof Note that if $\delta < 0.5$, then the term of P_k/α in (6) will converge to zero, i.e.,

$$\lim_{k\to\infty} \left| \frac{P_k}{\alpha} \right| = \lim_{k\to\infty} \left| \frac{1}{\alpha} \prod_{i=0}^{k-1} \frac{F_{i,n}}{F_i^*} \right| = 0. \tag{9}$$

In terms of (6), with the increase of the number of iterations, the ratio of the iterative control current to the desired current is

$$\frac{I_\infty}{I_{\infty,d}} = \lim_{k\to\infty}\frac{I_k}{I_{k,d}} = \lim_{k\to\infty}\frac{G_d}{G_d(1+S_k)+P_k/\alpha}\ . \tag{10}$$

While P_k/α converges to zero, the ratio of iterative control current to desired current is

$$\frac{I_\infty}{I_{k,d}} = \frac{1}{1+S_\infty}\ . \tag{11}$$

Assume that $\delta \le \varepsilon < 0.5$, where ε is a given constant, then

$$\begin{aligned}|S_\infty| &= \lim_{k\to\infty}\left|\sum_{j=1}^{k-1}\prod_{i=1}^{j}\frac{F_{k-i,n}}{F^*_{k-i}}\right| \\ &\le \lim_{k\to\infty}\sum_{j=1}^{k-1}\left|\prod_{i=1}^{j}\frac{F_{k-i,n}}{F^*_{k-i}}\right| \\ &\le \sum_{k=1}^{\infty}\varepsilon^k\ .\end{aligned} \tag{12}$$

As $\sum_{k=0}^{\infty}\varepsilon^k = \frac{1}{1-\varepsilon}$ while $\varepsilon \in (0, \frac{1}{2})$, (12) can be written as

$$|S_\infty| \le \sum_{k=1}^{\infty}\varepsilon^k = \frac{\varepsilon}{1-\varepsilon},\ \ \varepsilon \in (0,1)\ . \tag{13}$$

That is, while $\varepsilon \in (0, \frac{1}{2})$, $|S_\infty| \le 1$.

Suppose that the system output F_k is

$$F_k = F_{k,r} + F_{k,n}\ . \tag{14}$$

In terms of (4) and (5), the relative tracking error of the system is

$$\begin{aligned}\lim_{k\to\infty}\left|\frac{F_k - F_k^*}{F_k^*}\right| &= \lim_{k\to\infty}\left|\frac{F_{k,r}+F_{k,n}-F_k^*}{F_k^*}\right| \\ &\le \lim_{k\to\infty}\left|\frac{G_d}{G_d}\right|\left|\frac{I_k - I_{k,d}}{I_{k,d}}\right| + \left|\frac{F_{k,n}}{F_k^*}\right|.\end{aligned} \tag{15}$$

Considering (6) and (11), the relative tracking error of the system can be written as

$$\begin{aligned}\lim_{k\to\infty}\left|\frac{F_k - F_k^*}{F_k^*}\right| &\le \lim_{k\to\infty}\left|\frac{I_k}{I_{k,d}} - 1\right| + \varepsilon \\ &= \left|\frac{S_\infty}{1+S_\infty}\right| + \varepsilon.\end{aligned} \tag{16}$$

Due to (12) and (13), while $0 < \varepsilon < \frac{1}{2}$, the relative tracking error is

$$\begin{aligned}\lim_{k\to\infty}\left|\frac{F_k - F_k^*}{F_k^*}\right| &= \left|\frac{S_\infty}{1+S_\infty}\right| + \varepsilon \\ &\le \frac{|S_\infty|}{1-|S_\infty|} + \varepsilon \\ &\le \frac{\varepsilon/(1-\varepsilon)}{1-\varepsilon/(1-\varepsilon)} + \varepsilon \\ &= \frac{2\varepsilon(1-\varepsilon)}{1-2\varepsilon}.\end{aligned} \tag{17}$$

Since $\left(\frac{2\varepsilon(1-\varepsilon)}{1-2\varepsilon}\right)' = 1 + \frac{1}{(1-2\varepsilon)^2} > 0$, $\frac{2\varepsilon(1-\varepsilon)}{1-2\varepsilon}$ will decrease accordingly as ε decreases.

Furthermore,

$$\lim_{\varepsilon\to 0}\frac{2\varepsilon(1-\varepsilon)}{1-2\varepsilon} = 0\ . \tag{18}$$

That is, the smaller the value of δ, the more significant improvement of system tracking performance. As the value of δ is close to zero, the system's relative tracking error is close to zero.

Note that proof of Theorem 1 in [11] and Lemma 1 in this paper show that the MIIFC scheme works for nonlinear single-input single-output control systems as well. □

Remark 1 Lemma 1 shows that the MIIFC scheme has a strong ability of uncertainty attenuation.

4 Experimental results

In order to verify the effectiveness of the MIIFC scheme designed in this paper, the damping force tracking experiments of the MR damper are carried out. The parameter of α is set as 0.9. DYMH-106 pressure sensor is installed in the seat suspension experimental system, which accuracy is $0.003N$. In order to test the ability of disturbance attenuation of the designed MIIFC scheme, random error with mean 0 and the standard deviation $0.003N$ is added to the output of the damping force.

Figures 5, 6, 7, 8, 9, 10 and 11 show the simulation results of damping force tracking experiment, where the desired damping force is manually specified to test the tracking performance of the proposed algorithm. The maximum value of the tracking error in Fig. 10 is less than $0.2kN$, and the maximum error percentage (maximum error divided by maximum damping force of $2.5kN$) is about 6.068%, which show that reference signals can be effectively tracked with the MIIFC scheme.

The desired frequency signal in Fig. 11 has a large range of variation over a short period of time. Due to the hysteresis characteristics of the MR damper, the tracking error at the early stage cannot converge quickly. The tracking error gradually converges to and the fluctuation is within the range of $(-0.1, +0.1)kN$.

Table 2 shows the maximum error and the mean square error (MSE) during the first and second iterations, and the error percentage of MR damper when tracking desired signals at different frequencies. It can be seen that the MSE of the first iteration is much larger than that of the second iteration. Furthermore, for low-frequency signals, for example, 0.1 Hz, 0.5 Hz, 1 Hz, the MSE is reduced from the level of 10^{-2} to 10^{-3}, i.e., the tracking performance of low-frequency signals improves significantly by the MIIFC scheme along iterations. For high-frequency signals (3 Hz and 5 Hz) and the two complex frequency signals, the MSE is not greatly reduced along iterations. Although the MSE increases for higher frequency signals, the MSE fluctuates are still around level of 10^{-3}, i.e., effective tracking of the desired signal can be achieved by the MIIFC scheme.

5 Physics experiment

The effectiveness of the proposed control strategy has been verified through simulation experiments. In this section, further physics experiments are carried out, and the desired damping force is calculated by the upper-level controller according to the test road surface. In practical applications, the primary method for controlling MR dampers is the inverse model control strategy[13,17,20]. To validate the practical viability of the MIIFC scheme, we conducted a comparative analysis against the double-hidden-layer BP neural network inverse model of the MR damper as established in [18]. In the inverse model of the MR damper as shown in Fig. 12, the input layer has 3 nodes, representing the damping force F, piston displacement S, and piston velocity v at the current moment, respectively. The output layer has 1 node, representing the current I at that moment. Both hidden layers contain 12 neurons. The data used to train the neural network was obtained from real physical experiments. The tangential sigmoid transfer function (tansig) and linear function (purelin) are selected as the transfer functions for the hidden layer and output layer, respectively. The Levenberg-Marquardt algorithm (function trainlm), known for its fast convergence, is chosen as the training algorithm. The training function learngdm, which includes a momentum term, is used, and the mean squared error between the neural network's predicted output and actual output is taken as the performance metric for the neural network. Damping force tracking experiments are conducted under three distinct road conditions, namely sinusoidal, bump and random road surfaces. Additionally, the impact of temperature changes within the MR damper on its control effectiveness is taken into consideration.

5.1 Results obtained under different road surfaces

Tracking experiments of the damping force are conducted on a sinusoidal road surface with a frequency of $2Hz$ and an amplitude of $0.05m$. The experimental results under this operating condition are shown in Fig. 13. In Fig. 13a, the blue solid line represents the height variation curve of the sinusoidal road surface. In Fig. 13b, the red solid line represents the desired damping force, the blue dotted line represents the output damping force with the MIIFC scheme, and the black dotted line represents the output damping force with only inverse model control.

Tracking experiments of damping force are conducted with a speed of $10km/h$ passing through a bump with a width of $1m$ and a height of $0.04m$, and the experimental results are shown in Fig. 14. In Fig. 14a, the blue solid line represents the height variation curve of the bump road surface. In Fig. 14b, the red solid line represents the desired damping force, the blue dotted line represents the output damping force with the

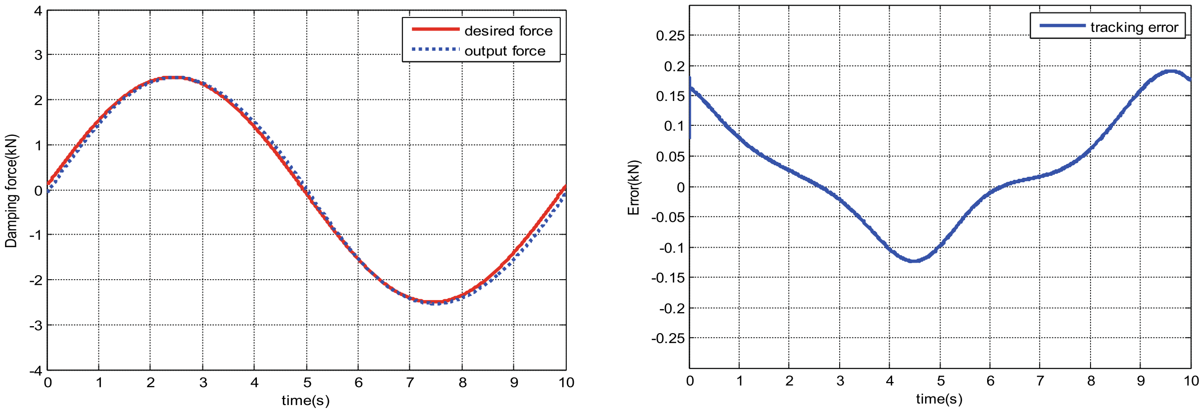

(a) tracking curve. (b) error curve.

Fig. 5 Tracking curve and error curve of damping force ($f = 0.1$ Hz). Solid line: the desired damping force, dashed line: the damping force generated by the MIIFC

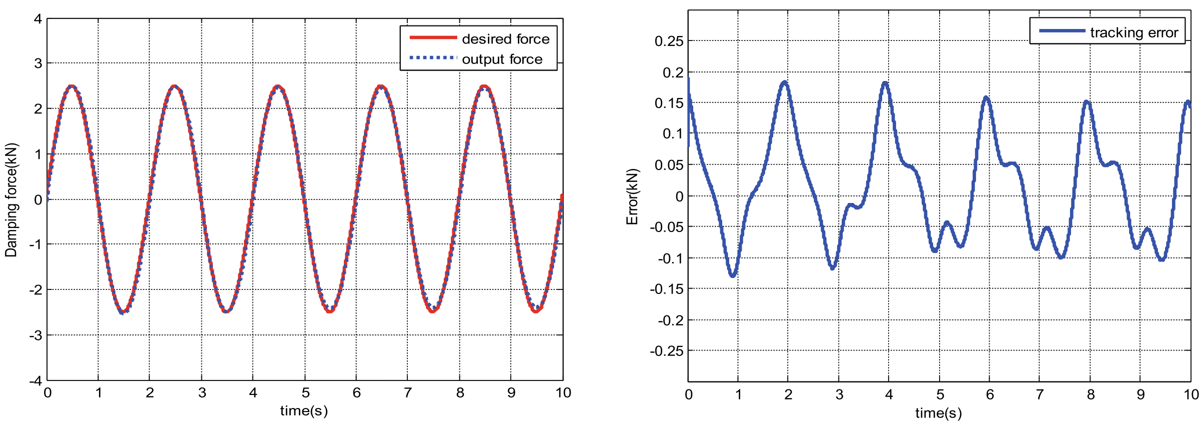

(a) tracking curve. (b) error curve.

Fig. 6 Tracking curve and error curve of damping force ($f = 0.5$ Hz). Solid line: the desired damping force, dashed line: the damping force generated by the MIIFC

Table 2 Maximum error, error percentage, mean square error while tracking desired signals

Frequency (Hz)	First iteration MSE(kN^2)	Second iteration MSE(kN^2)	Max error (kN)	Percentage (%)
0.1	0.0170	0.0011	0.0785	3.1411
0.5	0.0176	0.0032	0.1421	4.8812
1	0.0184	0.0079	0.1989	7.9550
3	0.0226	0.0131	0.2433	9.7337
5	0.0280	0.0220	0.2871	11.4823
(0.5,3)	0.0587	0.0093	0.1646	6.5828
(0.5,1,3)	0.0243	0.0045	0.1696	6.7848

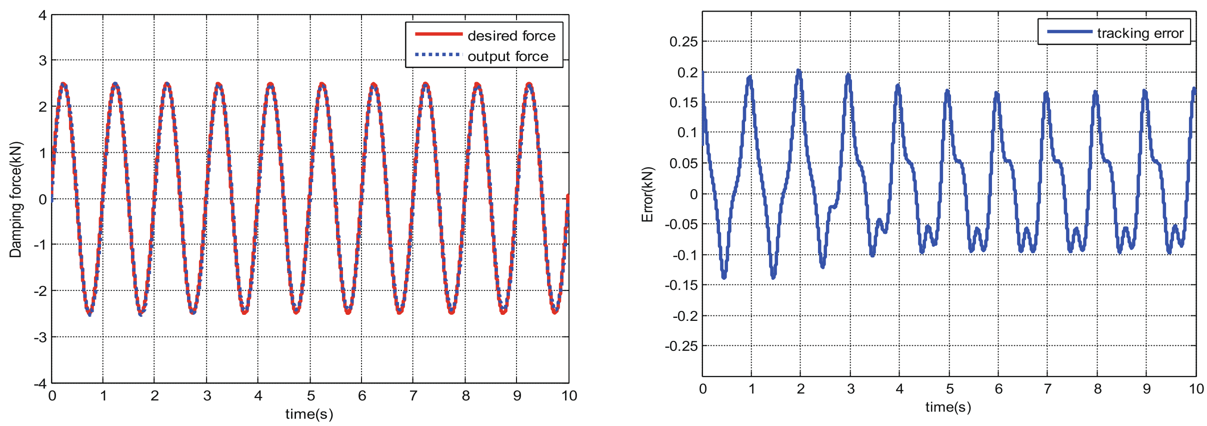

(a) tracking curve.

(b) error curve.

Fig. 7 Tracking curve and error curve of damping force ($f = 1\,\mathrm{Hz}$). Solid line: the desired damping force, dashed line: the damping force generated by the MIIFC

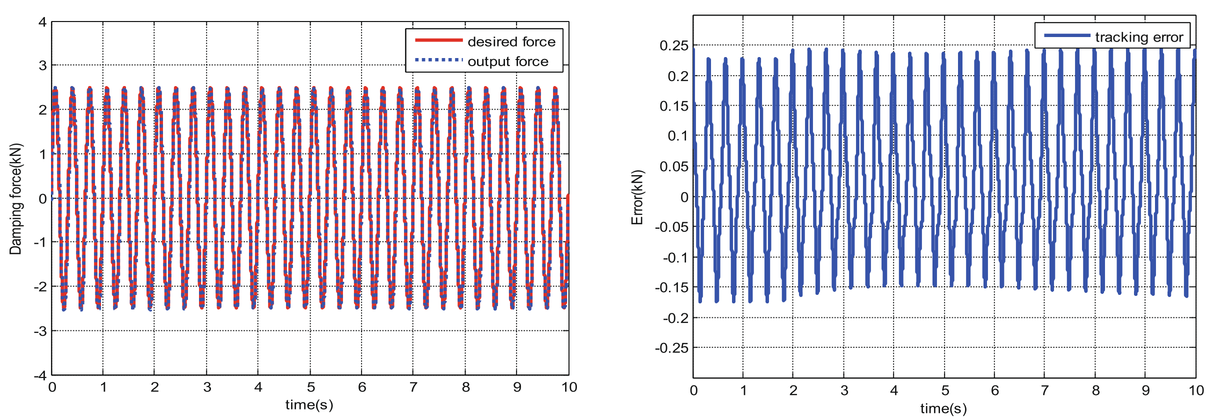

(a) tracking curve.

(b) error curve.

Fig. 8 Tracking curve and error curve of damping force ($f = 3\,\mathrm{Hz}$). Solid line: the desired damping force, dashed line: the damping force generated by the MIIFC

MIIFC scheme, and the black dotted line represents the output damping force with only inverse model control.

Meanwhile, tracking experiments of damping force are conducted on a Class C road. According to the Chinese National Standard (GB/T 7031-2005), the road surface is divided into 8 classes, from Class A to Class H. The Class C road selected in this paper usually refers to the lower standard secondary roads or rural roads which are suitable for testing the performance of semi-active suspension. The experimental results are shown in Fig. 15. In Fig. 15a, the blue solid line represents the height variation curve of the random road surface. In Fig. 15b, the red solid line represents the desired damping force, the blue dotted line represents the output damping force with the MIIFC scheme, and the black dotted line represents the output damping force with only inverse model control.

The maximum error and MSE of the results of damping force tracking experiments with the above two methods are shown in Tables 3 and 4.

Based on Tables 3 and 4, both the proposed MIIFC scheme and the inverse model control can achieve satisfied tracking performance of the given damping force.

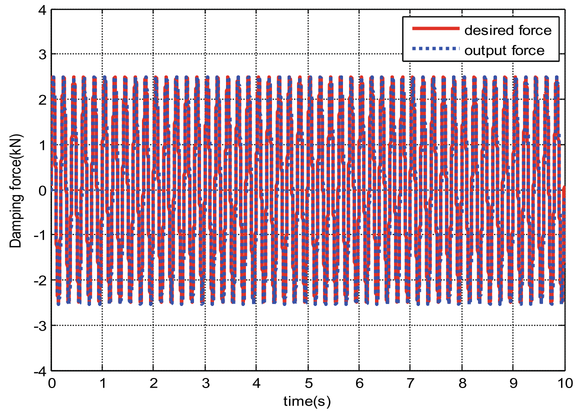

(a) tracking curve.

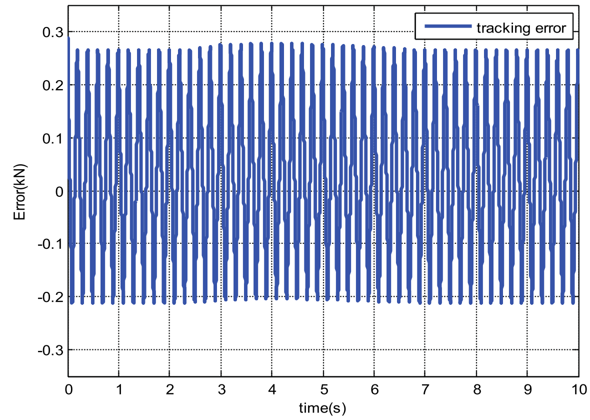

(b) error curve.

Fig. 9 Tracking curve and error curve of damping force ($f = 5$ Hz). Solid line: the desired damping force, dashed line: the damping force generated by the MIIFC

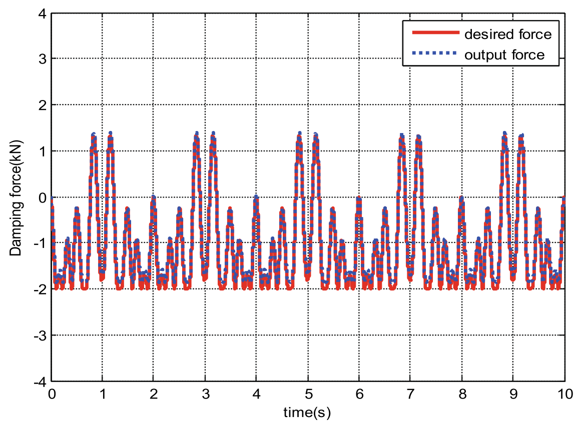

(a) tracking curve.

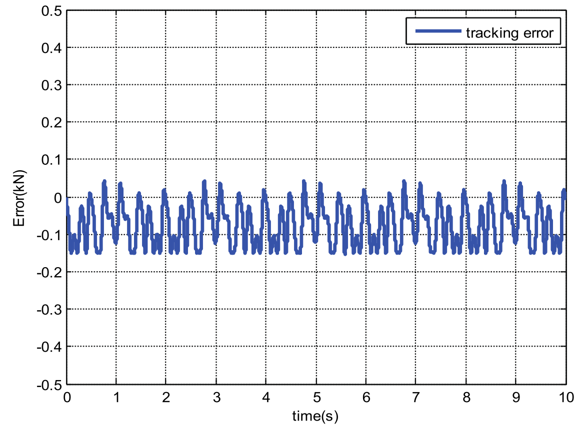

(b) error curve.

Fig. 10 Tracking curve and error curve of damping force ($f = (0.5, 3)$ Hz). Solid line: the desired damping force, dashed line: the damping force generated by the MIIFC

Table 3 Maximum error, mean square error with the MIIFC scheme while tracking desired signals

Simulated road surface	Max error (kN)	MSE (kN)^2
Sinusoidal	0.1526	3.1137×10^{-3}
Bump	0.0707	4.5109×10^{-4}
Random	0.2327	7.7216×10^{-3}

Table 4 Maximum error, mean square error with an inverse model control method while tracking different road surfaces

Simulated road surface	Max error/kN	MSE/$(kN)^2$
Sinusoidal	0.1519	5.2369×10^{-3}
Bump	0.0831	7.2555×10^{-4}
Random	0.2374	8.8153×10^{-3}

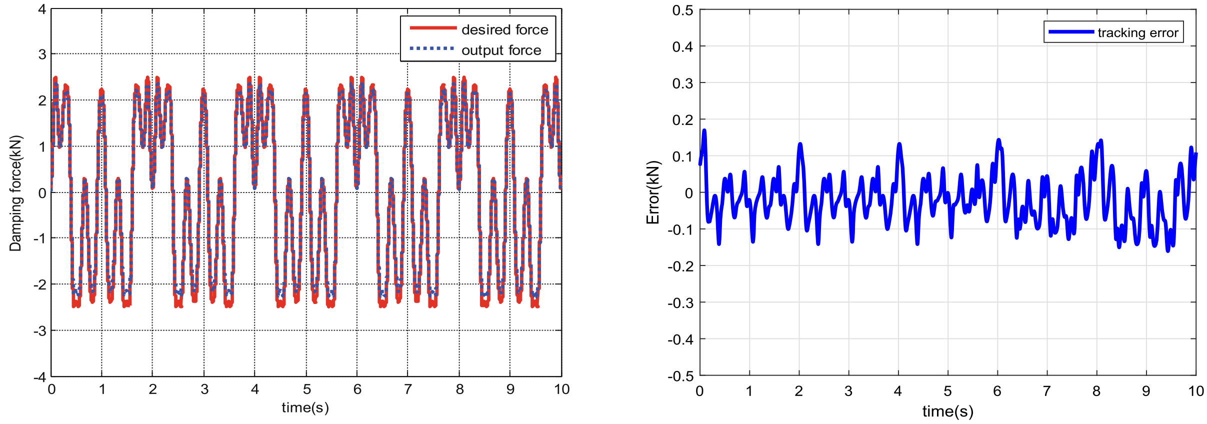

(a) tracking curve. (b) error curve.

Fig. 11 Tracking curve and error curve of damping force ($f = (0.5, 1, 3)$ Hz). Solid line: the desired damping force, dashed line: the damping force generated by the MIIFC

Fig. 12 The inverse model of the MR damper

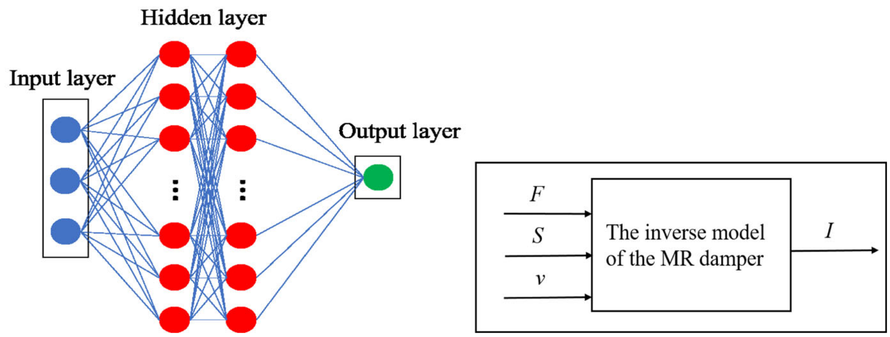

(a) Structure of the BP neural network. (b) Structure of the inverse model controller.

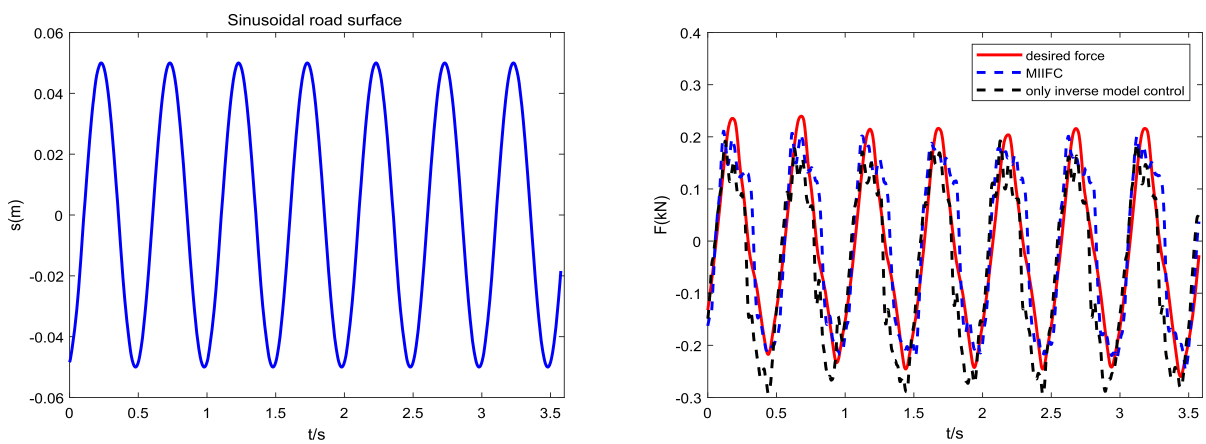

(a) Sinusoidal road surface. (b) The tracking curve.

Fig. 13 Results of the damping force tracking for a sinusoidal road surface

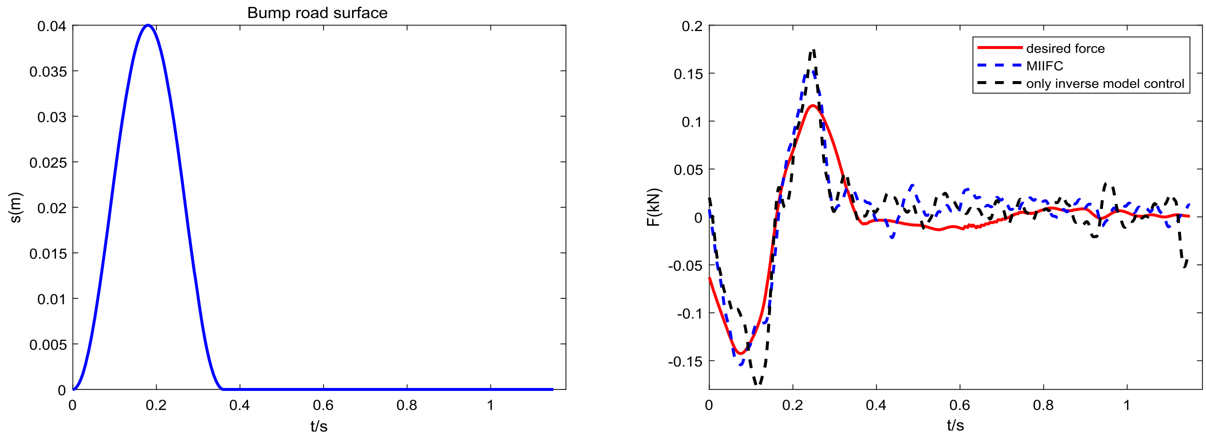

(a) Bump road surface. (b) The tracking curve.

Fig. 14 Results of the damping force tracking for a bump road surface

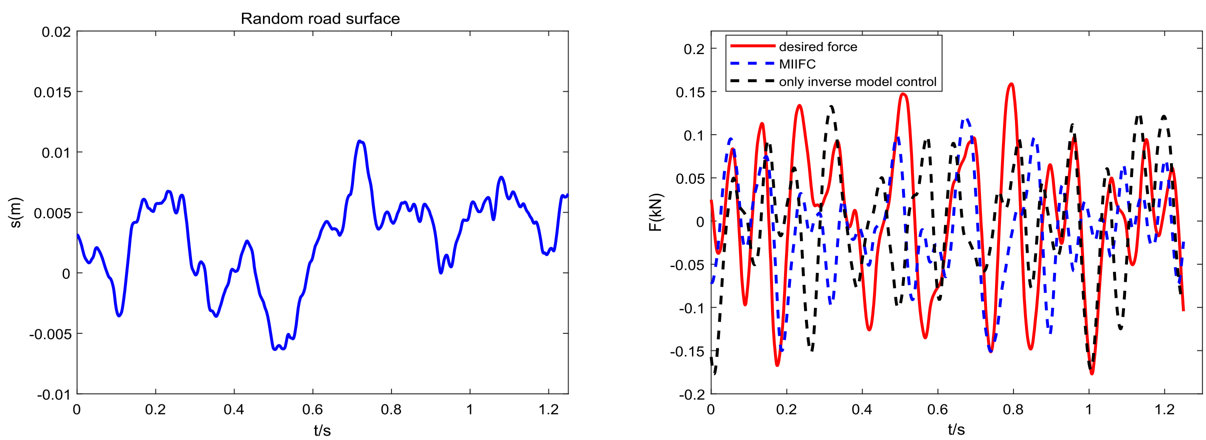

(a) Random road surface. (b) The tracking curve.

Fig. 15 Results of the damping force tracking for a random Class C road surface

5.2 Influence of temperature variations on MR damper

The inverse model control is widely used in the control of the magneto-rheological damping force. However, open-loop control is difficult to deal with disturbances. Furthermore, when an MR damper is continuously energized, changes in temperature can affect both the magnetic and electrical properties of the MR fluid, which in turn influence the magnetorheological damping coefficient, and eventually may lead to the mismatch of the inverse model. Comparative experiments considering the influence of the temperature change are conducted under different road surfaces by continuously applying 1A current to the MR damper to heat up the MR damper [9]. The results of a tracking experimental of a given damping force are shown in Figs. 16, 17 and 18.

In Fig. 16a, the blue solid line represents the curve of the sinusoidal road surface. In Fig. 16b, the red solid line represents the desired damping force, the blue dotted line represents the output damping force of the MIIFC scheme, and the black dotted line represents the output damping force with only an inverse model control.

In Fig. 17a, the blue solid line represents the curve of the bump road surface. In Fig. 17b, the red solid line represents the desired damping force, the blue dotted

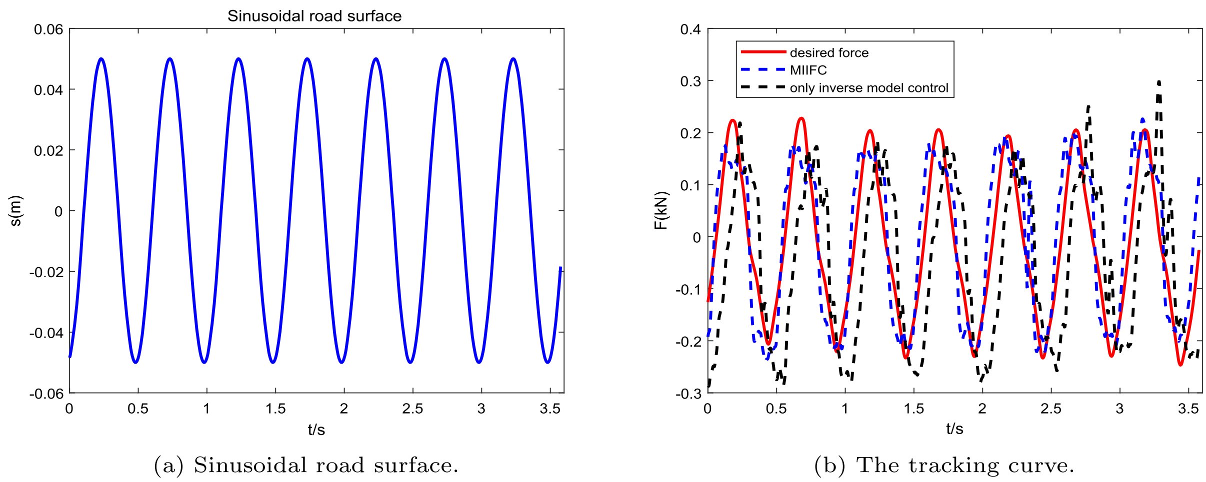

(a) Sinusoidal road surface. (b) The tracking curve.

Fig. 16 Results of the damping force tracking with the heated MR damper for sinusoidal road surface

Table 5 Maximum error, mean square error with the MIIFC scheme with the heated MRD while tracking different road surfaces

Simulated road surface	Max error (kN)	MSE (kN)^2
Sinusoidal	0.1796	4.2064×10^{-3}
Bump	0.0831	6.6847×10^{-4}
Random	0.2371	9.1401×10^{-3}

Table 6 Maximum error, mean square error with an inverse model control method with the heated MRD while tracking different road surfaces

Simulated road surface	Max error (kN)	MSE (kN)^2
Sinusoidal	0.2930	1.9432×10^{-2}
Bump	0.2660	1.9204×10^{-3}
Random	0.2598	1.2971×10^{-2}

line represents the output damping force of the MIIFC scheme, and the black dotted line represents the output damping force with only an inverse model control.

In Fig. 18a, the blue solid line represents the curve of the random road surface. In Fig. 18b, the red solid line represents the desired damping force, the blue dotted line represents the output damping force of the MIIFC scheme, and the black dotted line represents the output damping force with only an inverse model control.

Results of the maximum error and MSE for damping force tracking experiments with the heated MR damper by the above two methods are shown in Tables 4 and 5. Note that the control currents applied in all of these experiments are constrained within the range of 0 to 1A.

Tables 3, 4, 5 and 6 show that the inverse model control leads to a significant reduction in tracking accuracy after the MR damper heats up. The proposed MIIFC scheme can effectively attenuate model mismatch of the inverse model, and achieve satisfied tracking performance that MSEs are less than 10^{-3}.

5.3 Performance evaluation of seat suspension with an MR damper

The robustness of the MIIFC scheme was evaluated on a successive bump road surface with an MR damper at high temperature conditions. Note that there are no temperature sensors on the testbed for the MR damper, its precise temperature cannot be directly measured. Applying the maximum current allowed by the testbed (1A) to the MR damper for 3 min leads to a significant rise in the fluid temperature, which in turn affects the damping characteristics of the system [9]. The performance of the seat suspension system is presented in Figs. 19, 20 and 21.

At a velocity of 10 km/h, traversing successive bumps with heights of 0.04m and 0.06m, the time-domain response of the seat suspension system is depicted in Fig. 19. Figure 19b illustrates the vertical acceleration of the seat, showcasing that the MIIFC scheme exhibits slightly superior performance compared to the other two methods. Figure 19c illus-

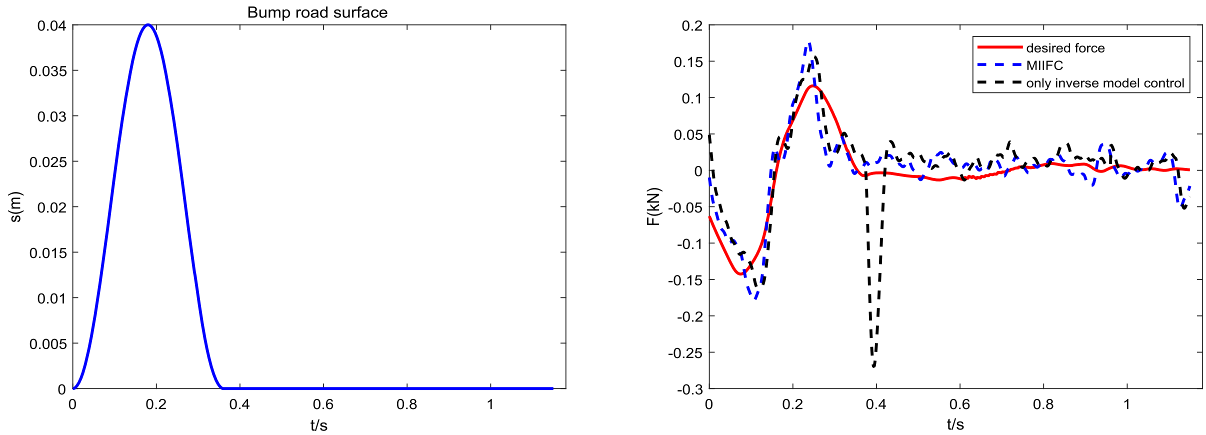

(a) Bump road surface.

(b) The tracking curve.

Fig. 17 Results of the damping force tracking with the heated MR damper for bump road surface

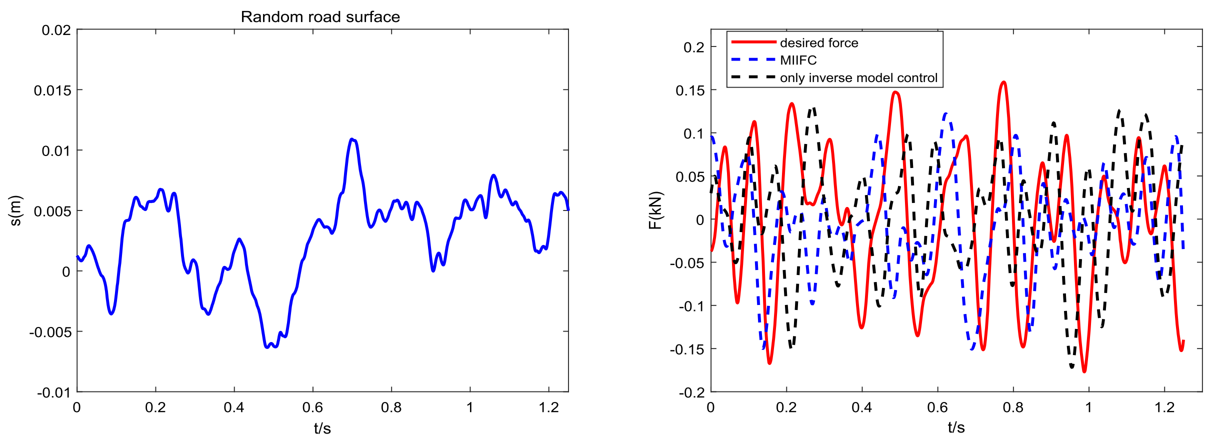

(a) Random road surface.

(b) The tracking curve.

Fig. 18 Results of the damping force tracking with the heated MR damper for random road surface

trates the damping force tracking curve, revealing temperature-induced model mismatches at 0.45s and 0.95s. The force tracking performance of the inverse model control is inadequate, resulting in significant fluctuations in the suspension stroke, as depicted in Fig. 19d. In contrast, the MIIFC scheme can effectively track the desired damping force, ensuring the ride comfort of the seat suspension system.

When the vehicle velocity increases to 30 km/h, the timedomain response of the seat suspension system is depicted in Figs. 20 and 21. It is observed that the inverse model method fails to adequately track the damping force, resulting in suboptimal ride comfort compared to passive suspension strategy. In contrast, the MIIFC scheme demonstrates consistent force tracking performance and presents notable advantages in enhancing ride comfort. In conclusion, the presence of temperature variations, fluctuations in MR fluid performance, and other system parameter variations may lead to model mismatches and a deterioration in damping force tracking accuracy within inverse model control scheme. Nevertheless, experimental evaluations conducted on a testbed equipped with an MR damper under varying temperature conditions confirmed the robustness of the MIIFC scheme in enhancing seat suspension performance under realistic operating scenarios. The maximum acceleration and root mean square results of

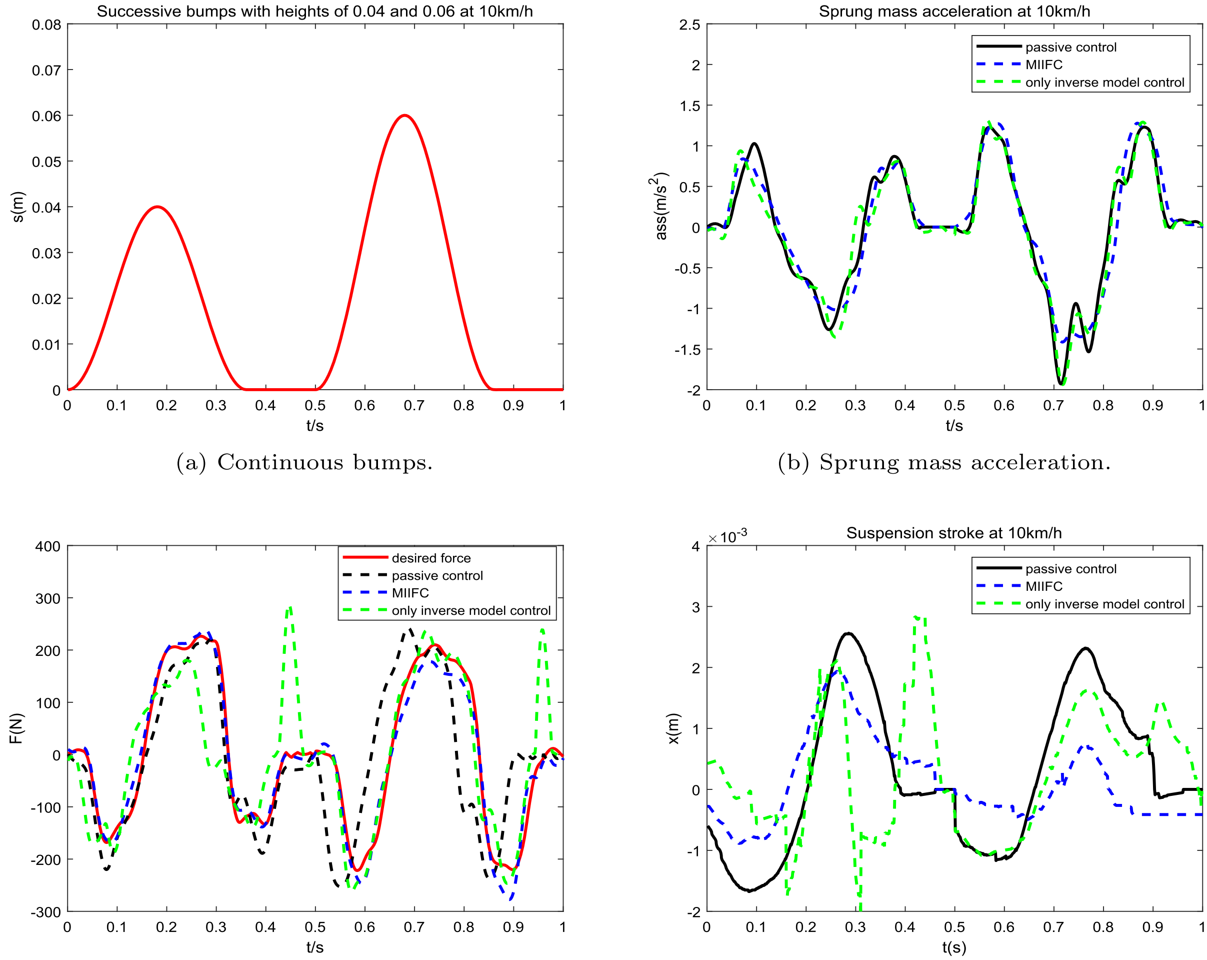

(a) Continuous bumps.

(b) Sprung mass acceleration.

(c) Damping force.

(d) Suspension stroke.

Fig. 19 Time-domain response of the seat suspension at a speed of 10 km/h

Table 7 Maximum acceleration, root mean square at a speed of 10 km/h

Method	Max acceleration (m/s^2)	RMS (m/s^2)
Passive control	1.9297	0.3272
MIIFC	1.4146	0.3232
Only inverse model control	1.938	0.3238

Table 8 Maximum acceleration, root mean square at a speed of 30 km/h

Method	Max acceleration (m/s^2)	RMS (m/s^2)
Passive control	7.3471	0.923
MIIFC	5.4609	0.6901
Only inverse model control	7.498	1.0272

the vertical seat at two speeds are shown in Tables 7, 8 and 9.

As shown in Table 7, for the test speed of 10 km/h, the RMS value of the sprung mass acceleration with the proposed method is slightly lower. However, from the damping force tracking curve, it can be observed that due to the model mismatch, the inverse model control struggles to accurately track the desired damping force.

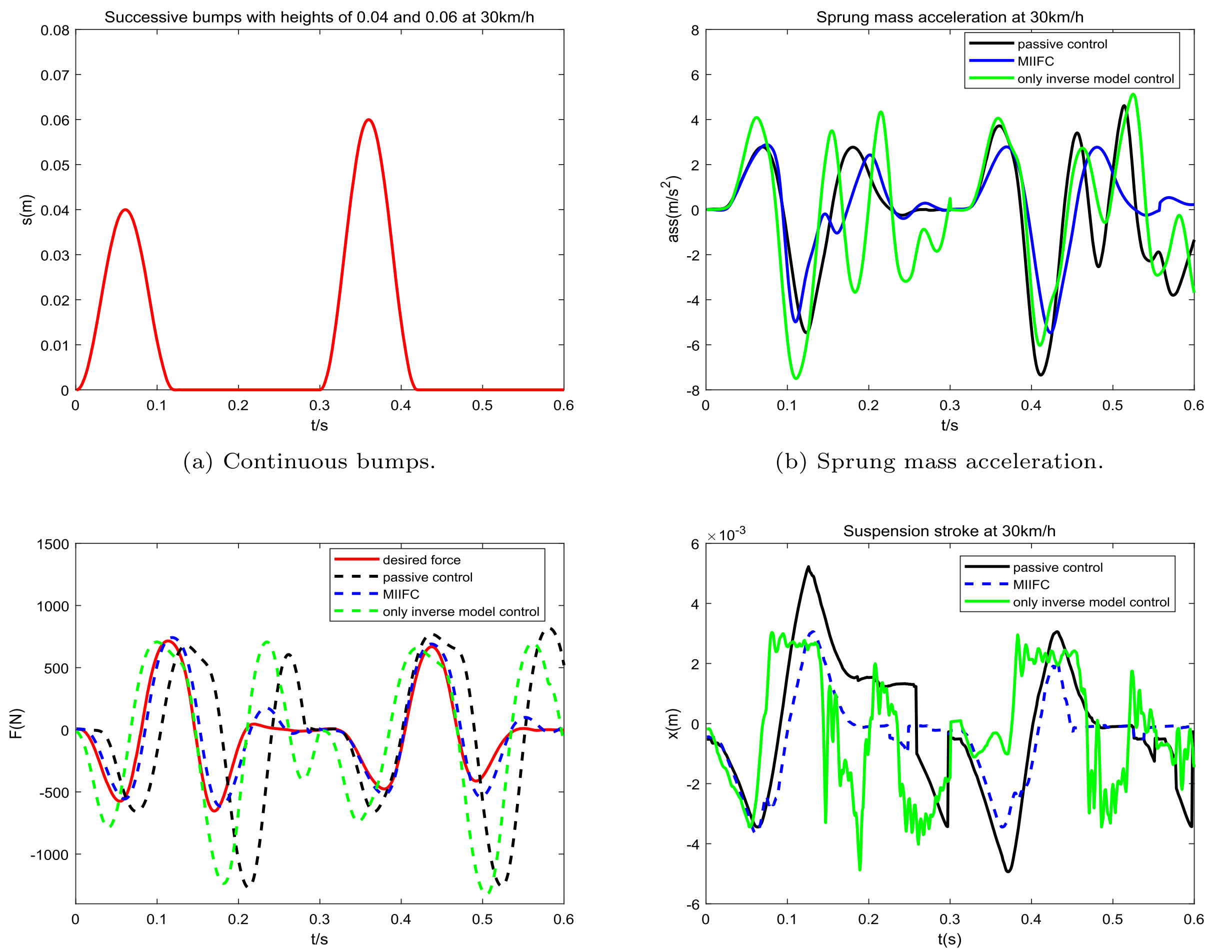

(a) Continuous bumps.

(b) Sprung mass acceleration.

(c) Damping force.

(d) Suspension stroke.

Fig. 20 Time-domain response of the seat suspension at a speed of 30 km/h

Table 9 Maximum acceleration, root mean square at a speed of 30 km/h

Method	Max acceleration (m/s^2)	RMS (m/s^2)
Passive control	5.347	2.276
MIIFC	2.651	1.117
Only inverse model control	7.078	2.307

As shown in Tables 8 and 9, for the test speed of 30 km/h, the RMS value of the sprung mass acceleration with the proposed method is significantly lower than those of the other two methods, which verifies the robustness of the proposed method under higher speeds and varying road conditions.

Remark 2 As shown in Tables 7, 8 and 9, the inverse model control demonstrates inferior performance compared to passive control. This outcome is reasonable, as the inverse model is more sensitive to temperature variations. An increase in temperature exacerbates the mismatch between the inverse model and the actual system, leading to a degradation in its performance relative to passive control.

Remark 3 Due to experimental safety guidelines, a wider temperature variation range was not allowed.

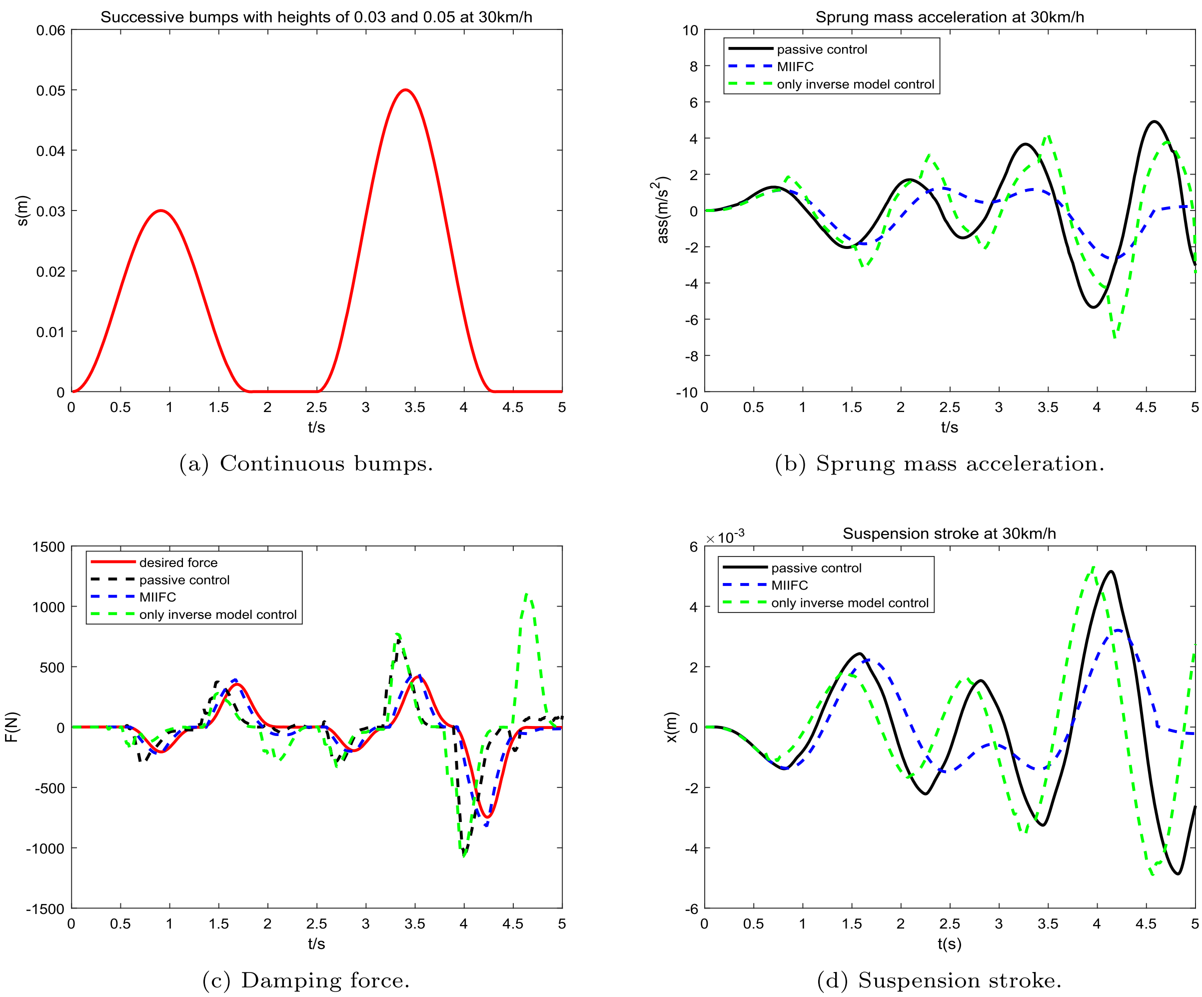

(a) Continuous bumps.

(b) Sprung mass acceleration.

(c) Damping force.

(d) Suspension stroke.

Fig. 21 Time-domain response of the seat suspension at a speed of 30 km/h

Therefore, the robustness of the proposed method was validated within a reasonable range of temperature changes.

6 Conclusion

This paper proposed a modeling-free inversion-based iterative feedforward control scheme for magnetorheological dampers. On one hand, MIIFC was designed as a data-driven approach, achieving system control solely through real-time input and output data. On the other hand, the iterative process effectively mitigated the impact of model uncertainties or external disturbances on system dynamics, thereby enhancing the robustness. Through simulations and experiments at different vehicle speeds and with various road excitations, the semi-active suspension system with the MIIFC strategy was shown to outperform both conventional passive suspension and semi-active suspension using the inverse model-based controller. Note that, different from [23], the proposed MIIFC fits for both linear and nonlinear SISO systems. Future research will focus on the improvement on tracking accuracy of desired damping force.

Author contributions Shaoyu Sun wrote the main manuscript text and Jie Guo completed the typographical correction of the article and the layout of the references, and Xinze Xu and Songlin Zhang prepared all figures. All authors reviewed the manuscript.

Funding This work is supported by the National Natural Science Foundation of China (No. 62473167) and the Natural Science Foundation of Jilin Province (No. 20240402079GH).

Data availibility No datasets have been used in this study.

Declarations

Conflict of interest The authors have no relevant financial or non-financial interests to disclose. Authors hereby declare that there are no conflict of interest.

References

1. Cheng, M., Chen, Z.B., Xing, J.W.: Design, Analysis, and Experimental Evaluation of a Magnetorheological Damper With Meandering Magnetic Circuit. IEEE Trans. Magn. **54**(5), 1–10 (2018)
2. Feng, Z., Ling, J., Ming, M., Xiao, X.: Precision motion control for a piezoelectric micro-positioning stage via integrating iterative learning and disturbance observer. Robot **40**(6), 59–68 (2018)
3. Guo, J., Li, Z., Zhang, M.: Parameter identification of the phenomenological model for magnetorheological fluid dampers using hierarchic enhanced particle swarm optimization. J. Mech. Sci. Technol. **35**(3), 875–887 (2021)
4. Hu, G., Qi, H., Chen, M., Yu, L., Li, G., Zheng, H.: Optimal design of magnetorheological damper with multiple axial fluid flow channels using BP neural network and particle swarm optimization methodologies. Int. J. Appl. Electromagnet Mech. **67**(3), 339–360 (2021)
5. Hu, G., Yi, F., Liu, H., Zeng, L.: Performance analysis of a novel magnetorheological damper with displacement self-sensing and energy harvesting capability. J. Vib. Eng. Technol. **9**(1), 85–103 (2021)
6. JB/T 13513-2018: Bench test methods of cylindrical shock absorber for low-speed vehicles. China Machinery Industry Federation, Beijing, China (2018)
7. Jeong, K., Choi, S.B.: Takagi?Sugeno Fuzzy Observer-Based Magnetorheological Damper Fault Diagnosis Using a Support Vector Machine. IEEE Trans. Control Syst. Technol. **30**(4), 1723–1735 (2022)
8. Jiang, R., Rui, X., Wang, G., Yang, F., Zhu, W., Wei, M.: "Design and modeling of an innovative magnetorheological fluid-elastomeric damper with compact structure. J. Intell. Mater. Syst. Struct. **31**(18), 2088–2100 (2020)
9. Kariganaur, A.K., Kumar, H., Arun, M.: Influence of temperature on magnetorheological fluid properties and damping performance. Smart Mater. Struct. **31**(5), 055018 (2022)
10. Kemerli, M., Engin, T.: Numerical analysis of a monotube mixed mode magnetorheological damper by using a new rheological approach in CFD. Rheol. Acta **60**(1), 77–95 (2021)
11. Kim, K., Zou, Q.: A Modeling-Free Inversion-Based Iterative Feedforward Control for Precision Output Tracking of Linear Time-Invariant Systems. IEEE/ASME Trans. Mechatron. **18**(6), 1767–1777 (2013)
12. Kumar, T., Kumar, R., Jain, S.C.: Numerical investigation of semi-active torsional vibration control of heavy turbo-generator rotor using magnetorheological fluid dampers. J. Vib. Eng. Technol. **9**(5), 967–981 (2021)
13. Li, C.X., Bai, X.X.: Precise real-time hysteretic force tracking of magnetorheological damper. Smart Mater. Struct. **29**(11), 119502 (2020)
14. Liu, G., Chen, R., Zhang, D., Zhou, H.: Model-free Adaptive Robust Control for Two Motor Drive System Based on Neural Network Inversion. Proc. of the CSEE **39**(3), 868–874+965 (2019)
15. Rahman, M., Ong, Z.C., Julai, S., Ferdaus, M.M., Ahamed, R.: A review of advances in magnetorheological dampers: their design optimization and applications. J. Zhejiang Univ.-Sci. A **18**(12), 991–1010 (2017)
16. Tusset, A.M., Janzen, F.C., Piccirillo, V., Rocha, R.T., Balthazar, J.M., Litak, G.: On nonlinear dynamics of a parametrically excited pendulum using both active control and passive rotational (MR) damper. J. Vib. Control **24**(9), 1587–1599 (2018)
17. Wang, X.L., Lv, H.F., Huang, J.Y., Liu, G.P.: Model-free feedforward/feedback control scheme for magnetorheological damper. J. ZheJiang Univ. (Eng. Sci.) **56**(5), 873–878 (2022)
18. Xu, M.: Research on road preview model predictive control strategy for magneto-rheological semi-active suspension. Jilin University (2021)
19. Xu, B., Zhao, Y., Deng, B., Du, Y., Wang, C., Ge, H.: Non-parametric nonlinear restoring force and excitation identification with Legendre polynomial model and data fusion. Struct. Health Monit. **21**(2), 264–281 (2022)
20. Yan, Y., Dong, L., Han, Y., Li, W.: A general inverse control model of a magneto-rheological damper based on neural network. J. Vib. Control **28**(7–8), 952–963 (2022)
21. Yoon, D., Kim, G., Choi, S.: Response time of magnetorheological dampers to current inputs in a semi-active suspension system: Modeling, control and sensitivity analysis. Mech. Syst. Signal Process. **146**, 106999 (2021)
22. Yu, X., Hou, Z., Polycarpou, M.M.: A data-driven ILC framework for a class of nonlinear discrete-time systems. IEEE Trans. Cybern. 1-15 (2021)
23. Yu, S., Li, J., Lu, X., Feng, Y., Sun, X.: Modeling-free inversion-based iterative feedforward control for piezoelectric actuators. Proc. of the 2021 American Control Conference (ACC), pp. 1396-1401 (2021)
24. Zhu, H., Rui, X., Yang, F., Zhu, W., Wei, M.: An efficient parameters identification method of normalized Bouc-Wen model for MR damper. J. Sound Vib. **448**, 146–158 (2019)